Supplementary Information (SI) for Energy & Environmental Science.
This journal is © The Royal Society of Chemistry 2025

High-Efficiency Moisture Energy Harvesting at -30 °C via Hybrid Solute Engineering

Lin Li*, Fagui Dong, Pengpeng Miao, Nan He, Bingsen Wang, Xisheng Sun, Jie Miao, Haonan Wang*, Dawei Tang

School of Energy and Power Engineering, Key Laboratory of Ocean Energy Utilization and Energy Conservation of Ministry of Education, Dalian University of Technology, Dalian, 116024, People's Republic of China.

*Corresponding author: E-mail: lilinnd@dlut.edu.cn (Lin Li), wanghaonan@dlut.edu.cn (Haonan Wang)

Experimental Section

1.1 Materials Acrylamide (AAm, neutral monomer), 2-Acrylamido-2-methyl-1-propanesulfonic acid (AMPS,99%), 2-hydroxy-4'-(2-hydroxyethoxy)-2-methylpropiophenone (≥98.0% HPLC, photoinitiator), and N,N'-methylenebisacrylamide (MBAA, chemical crosslinker), along with ethylene glycol (EG, antifreeze component), were all purchased from Aladdin Reagent Co., Shanghai. Lithium trifluoromethanesulfonate (LiOTF, antifreeze component) was obtained from Macklin Biochemical Co., Shanghai. All chemicals were used as received without further purification. Deionized water was used in all experiments.

1.2 Preparation of HSH To prepare the precursor solution, 3 g of acrylamide (AAm; Aladdin), 5 g of lithium trifluoromethanesulfonate (LiOTF; Macklin), 0.8 g of 2-acrylamido-2-methyl-1-propanesulfonic acid (AMPS; Aladdin), 0.0057 g of 2-hydroxy-4’-(2-hydroxyethoxy)-2-methylpropiophenone (UV-I; Aladdin), and 0.0037 g of N,N′-methylenebisacrylamide (MBAA; Macklin) were dissolved in a mixed solvent of 7 mL of deionized water and 7 mL of ethylene glycol. The mixture was stirred on a magnetic stirrer for 30 minutes until a clear solution was obtained.

The resulting clear solution was poured into a polytetrafluoroethylene mold of specific dimensions and subjected to ultraviolet irradiation at 365 nm with a power of 45 W for 40 minutes to complete the polymerization reaction. The preparation processes of SFH and SSH were similar to that of HSH, with the key differences being that SFH lacked both ethylene glycol and lithium trifluoromethanesulfonate, while SSH contained ethylene glycol but no lithium trifluoromethanesulfonate.

1.3 Preparation of HSH-MEG The HSH hydrogel was employed as the power-generating material. In the device, stainless steel electrodes coated with carbon black and graphite felt served as the electrodes. The HSH hydrogel was sandwiched between Al-mesh/C electrodes to construct a MEG device.

1.4 Uniaxial Tensile Tests Acrylic clamps were bonded to both ends of the samples using 406 adhesive to prevent slippage from the testing machine. The samples for uniaxial tensile tests were 1.5 cm wide, 5 cm high, and 0.2 cm thick. The tests were conducted under ambient conditions, with three to six samples tested each time. All samples were stretched using a universal electronic testing machine (XK-206s) at a speed of 100 mm/min. The stress applied to the hydrogels was calculated by dividing the applied force by the initial cross-sectional area (width × thickness). Strain was determined as the deformation length of the hydrogels divided by the original length. Toughness was calculated by integrating the area under the tensile stress-strain curves for each sample. The Young's modulus was obtained from the slope of the initial linear region (strain 5%-20%) of the stress-strain curves. Notably, low-temperature tests were conducted in a constant temperature and humidity chamber (DHS-GDJS-100B), with humidity maintained at approximately 50% RH.

1.5 Electrical Measurements Current-voltage measurements were performed using a Keithley 6510 multimeter. The temperature and humidity of the testing environment were controlled by a constant temperature and humidity chamber (DHS-GDJS-100B). Unless otherwise specified, all other tests were conducted at room temperature. Long-term operation tests at low temperatures were also performed in a constant temperature and humidity chamber.

1.6 Characterization Raman spectra were recorded using a Horiba France Sas Xplora Plus Raman spectrometer equipped with a 532 nm laser source. Hygroscopic isotherms at 25 °C under different

humidity conditions were measured using a dynamic water vapor adsorption analyzer (TA).The ionic conductivity of the hydrogels was measured in the frequency range of 20 MHz to 0.1 Hz using a broadband dielectric impedance spectrometer (Novocontrol Concept 80). Differential scanning calorimetry (DSC) was performed using a METTLER TOLEDO DSC3, from -150 °C to 30 °C, with a cooling rate of 5 K/min. The freezable water content (W_f, %) was calculated using the following equation:

$$W_f(\%) = \frac{\Delta H_m}{\Delta H_m^0 W_{H_2O}} = \frac{Q_{out}}{\Delta H_m^0}$$

Where ΔH_m is the crystallization enthalpy of freezable water obtained by integrating the exothermic peak from the DSC curve,ΔH0 m is the melting enthalpy of pure water, ΔH0 m = 333.5 J g^{-1}; W_{H2O} is the water content of the hydrogel, and Q_{out} is the exothermic heat released when freezing of the water occurs.

1.7 ECG Monitoring The ECG measurement system consisted of a power module integrated with HSH-MEG, a BMD101 analog front-end featuring a low-noise amplifier and an ADC converter (operating voltage 3.3V ± 10%, current 0.8 mA), a microcontroller-Bluetooth module with an internal antenna, and two Ag/AgCl electrodes. Tests were conducted under relaxed, walking, and jogging conditions at approximately -16 °C. Two Ag/AgCl electrodes were attached to the left and right fingers, respectively. Signals from both hands were differentially input to the low-noise amplifier for integration, filtering, and amplification. The conditioned signals were then digitized by the ADC and transmitted to a mobile application (PC, smartphone, or tablet) using Bluetooth.

1.8 Theoretical Calculations All calculations were performed using the Gaussian 16 software. Density functional theory (DFT) calculations employed the B3LYP functional combined with

Grimme's D3BJ dispersion correction.[1] Geometric optimization and frequency calculations were conducted with the 6-31G(d) basis set. Fully optimized structures were computed without constraints, and harmonic frequency calculations confirmed the absence of imaginary frequencies.[2] Final energies were refined using the larger 6-311+G(d,p) basis set.[3] Binding energy (E_b) was calculated as follows:

$$E_b = E_{Complex} - (E_{M1} + E_{M1})$$

$E_{Complex}$, E_{M1} and E_{M2} represent the energy of the complex and the energy of the interacting molecule, respectively.

Additionally, in this paper, the electrostatic potential distribution (ESP) on the surface of the molecules was analysed and plotted using the Multiwfn program in conjunction with the VMD visualisation software.[4–6] In order to reveal the weak interactions (e.g. hydrogen bonding) in the system, we used interaction region indicator (IRI) for the analysis and the IRI isosurfaces have been plotted by Multiwfn wavefunction analysis program in conjunction with VMD software. These isosurfaces show the different interaction regions, where the colours are differentiated according to the nature of the interactions, giving a visual representation of the strength and type of hydrogen bonding and other non-covalent interactions.[7]

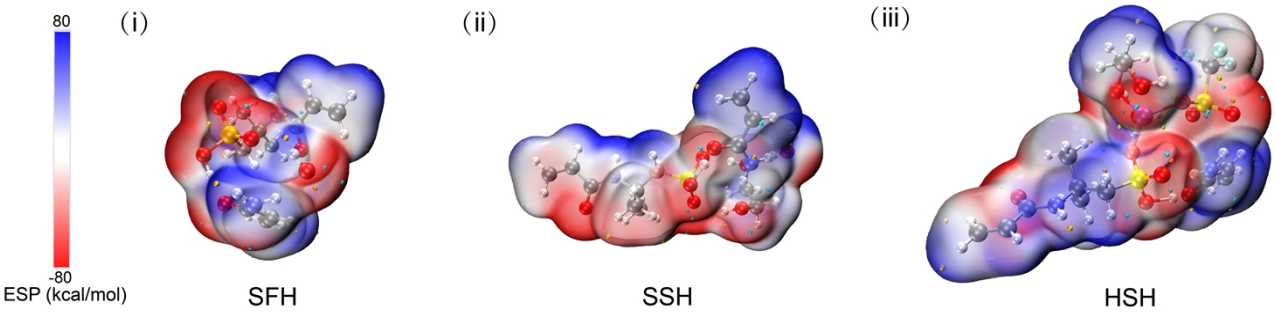

Fig. S1 The distribution of electrostatic potential (ESP) of SFH, SSH and HSH (from left to right) obtained through DFT calculations.

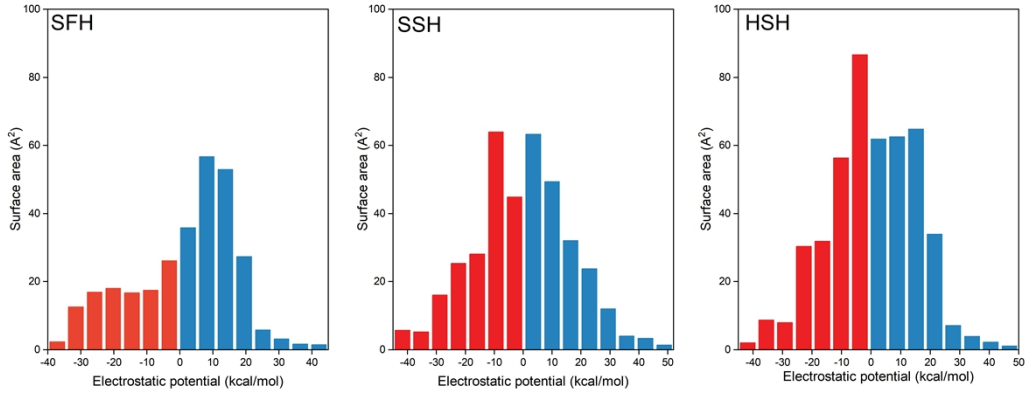

Fig. S2 Surface area corresponding to each ESP range on the van der Waals surface (vdW surface) of SFH, SSH, HSH.

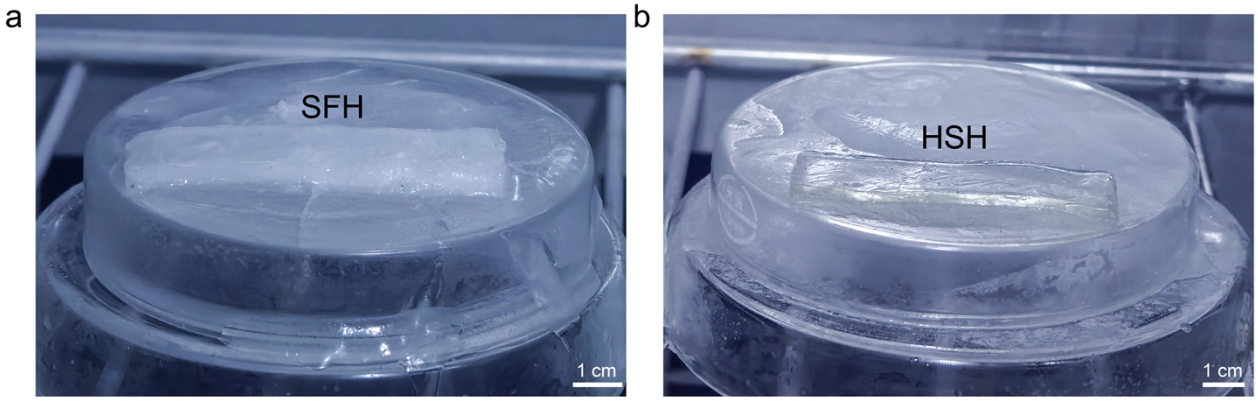

Fig. S3 Optical photographs of the hydrogel in an environment at -30 °C. (a) SFH; (b) HSH.

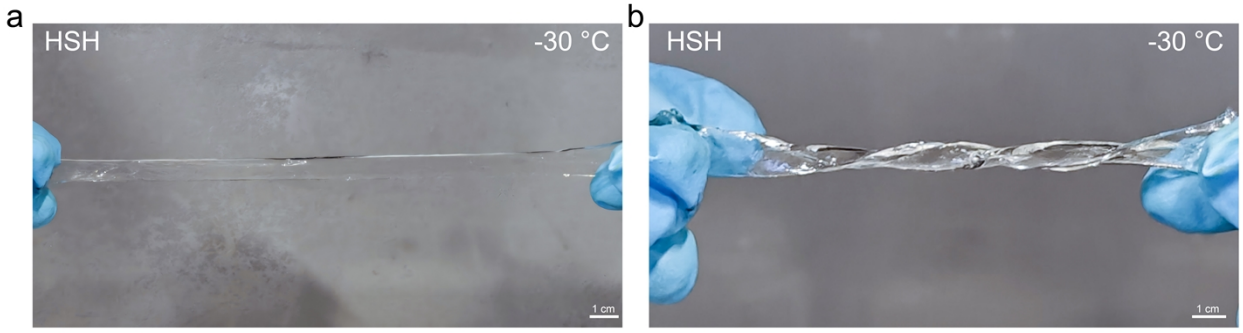

Fig. S4 Under the environment at -30 °C, HSH undergoes normal stretching and twisting. (a) Stretching; (b) Twisting.

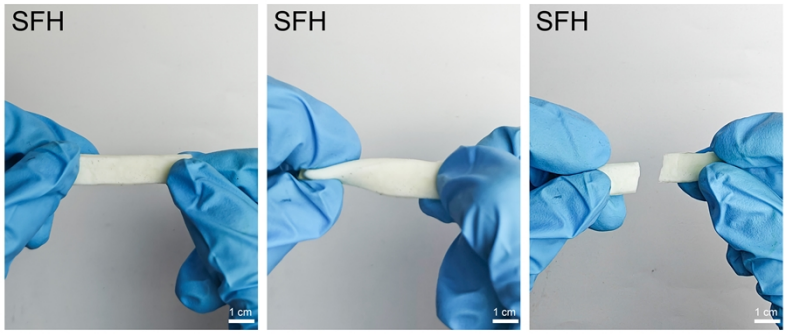

Fig. S5 Under the condition of -30 °C, SFH undergoes severe freezing and loses its stretchability and flexibility.

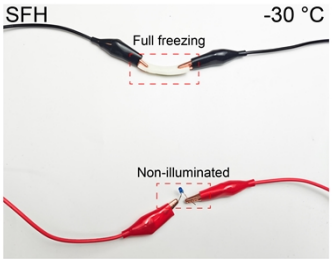

Fig. S6 Under the condition of -30 °C, SFH cannot act as a conductor to light up the LED light.

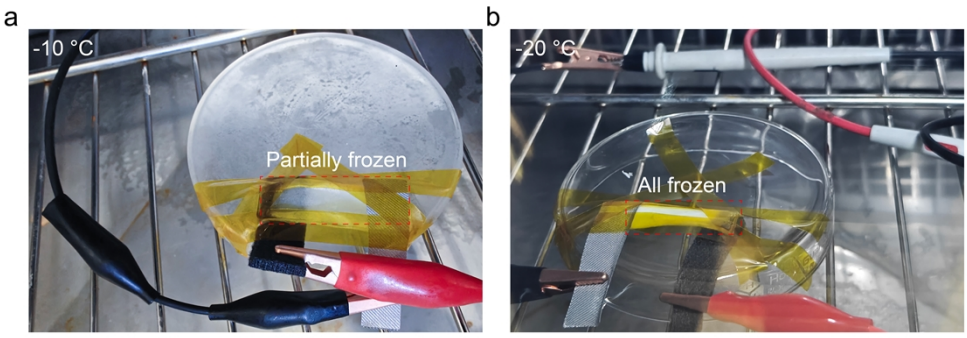

Fig. S7 The icing states of SFH-MEG in a low-temperature environment. (a) SFH-MEG undergoes partial freezing at -10 °C; (b) SFH-MEG undergoes complete freezing at -20 °C.

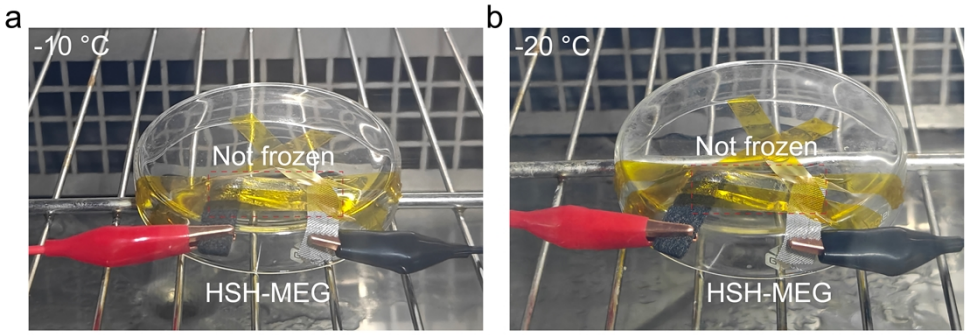

Fig. S8 The icing states of HSH-MEG in a low-temperature environment. (a) HSH-MEG did not undergo freezing at -10 °C; (b) HSH-MEG did not undergo freezing at -20 °C.

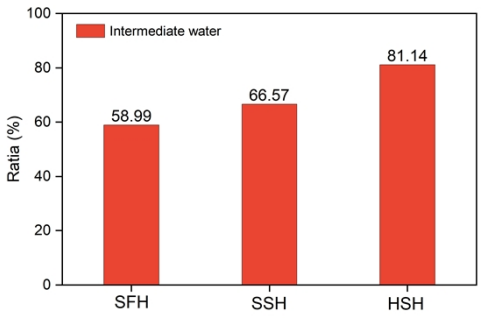

Fig. S9 The proportion of intermediate water in SFH, SSH and HSH.

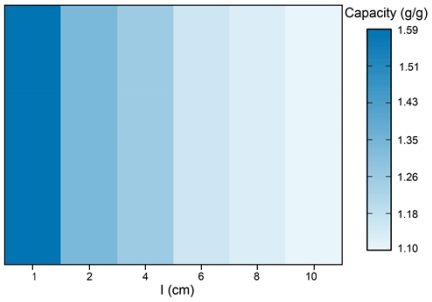

Fig. S10 The gradient distribution of water content in HSH-MEG after being placed in air for 48 hours.

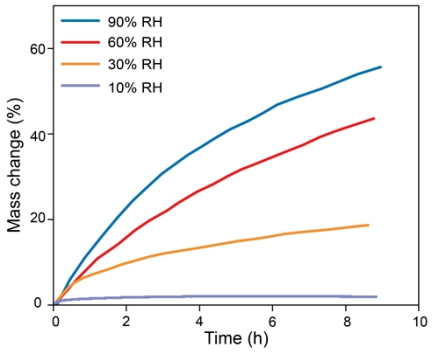

Fig. S11 Dynamic Vapor Sorption (DVS) curves display the dynamic moisture absorption process of HSH under different working conditions with relative humidities of 10%, 30%, 60% and 90% at 25 °C.

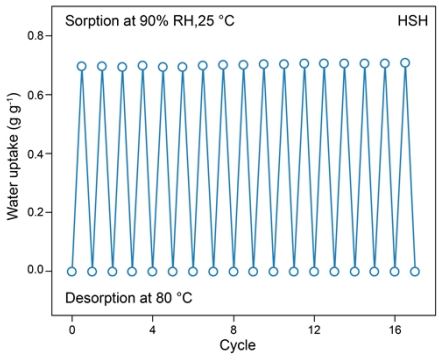

Fig. S12 Seventeen water sorption-desorption cycling tests were performed, with sorption at 25 °C and 90% RH and desorption at 80 °C, showing consistent cycling stability and no observable salt leakage.

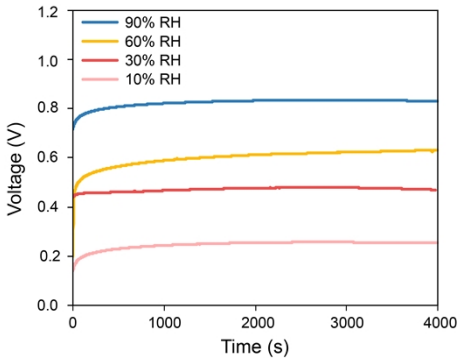

Fig. S13 Voltage of HSH-MEG with inert electrodes (C-Pt) at 25 °C and different humidity levels (10% RH, 30% RH, 60% RH, 90% RH).

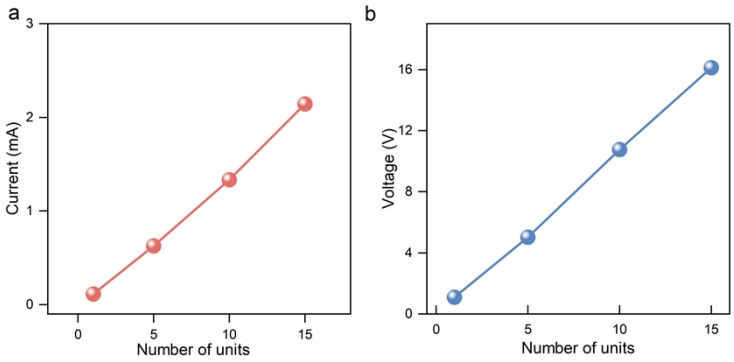

Fig. S14 Current and voltage increase with the number of HSH-MEG units connected in parallel or series.

Table. S1 Comparison of the low-temperature output performance of HSH-MEG with the reported moisture generation units.

Materials	Current density ($\mu A\ cm^{-2}$)	Temperature (°C)
PVA-AlgNa hydrogel[8]	13	-25
PVA-AlgNa hydrogel[8]	280	0
PVA-AlgNa hydrogel[8]	402	25
CNF/CNT aerogel[9]	26	-20
CNF/CNT aerogel[9]	30	0
CNF/CNT aerogel[9]	39	20
Mac-fabric[10]	40	-10
Mac-fabric[10]	128	10
Mac-fabric[10]	78	20
PVA-PA hydrogel[11]	54	-20
PVA-PA hydrogel[11]	131	0
PVA-PA hydrogel[11]	185	10
PVA-PA hydrogel[11]	274	20
Our work	86	-30
Our work	147	-20
Our work	221	-10
Our work	333	0
Our work	620	25

Table. S2 Comparison of ion conductivity between HSH and other antifreeze hydrogels at room temperature and low temperature.

Materials	Ion conductivity ($S\ m^{-1}$)	Temperature (°C)
EG-HANa[12]	1.32	25
EG-HANa[12]	0.57	0
EG-HANa[12]	0.12	-20
AMCl/EG[13]	0.81	-20
AMCl/EG[13]	1.55	25
PVA-SiO_2-2/LiCl[14]	5.61	25
PVA-SiO_2-2/LiCl[14]	0.75	-20
PAM-1,2-PG	2.96	25
PME[15]	1.65	20
PME[15]	0.19	-20
HE-30[16]	0.93	-20
HE-30[16]	1.08	0
HE-30[16]	1.45	25
PAM-2M $Zn(CF_3SO_3)_2$[17]	0.3	-30
PAM-2M $Zn(CF_3SO_3)_2$[17]	3.82	25
Our work	7.14	25
Our work	2.15	-30

Table. S3 Comparison of HSH-MEG with reported moisture generation units in terms of operating time and temperature adaptation range.

Materials	Duration (h)	Temperature (°C)
PVA-AlgNa hydrogel[8]	120	22
PVA-PA hydrogel[11]	144	15
Ionic nanocomposite[18]	80	20
SWNT/PVA/CNF aerogel[19]	120	20
Graphene oxide composite[20]	120	15
PSSA/R film[21]	50	10
PSSA-Kc film[22]	180	22
Nanofiber film[23]	120	25
PVA hydrogel[24]	150	21
Our work	243	-25

References

1 S. Grimme, S. Ehrlich and L. Goerigk, *J. Comput. Chem.*, 2011, **32**, 1456–1465.
2 W. J. Hehre, R. Ditchfield and J. A. Pople, *J. Chem. Phys.*, 1972, **56**, 2257–2261.
3 T. Clark, J. Chandrasekhar, G. W. Spitznagel and P. V. R. Schleyer, *J. Comput. Chem.*, 1983, **4**, 294–301.
4 T. Lu, *J. Chem. Phys.*, 2024, **161**, 082503.
5 T. Lu and F. Chen, *J. Comput. Chem.*, 2012, **33**, 580–592.
6 S. Manzetti and T. Lu, *J. Phys. Org. Chem.*, 2013, **26**, 473–483.
7 T. Lu and Q. Chen, *Chemistry–Methods*, 2021, **1**, 231–239.
8 S. Yang, L. Zhang, J. Mao, J. Guo, Y. Chai, J. Hao, W. Chen and X. Tao, *Nat. Commun.*, 2024, **15**, 3329.
9 E. Shin, G. Kim, K. Zhao, G. Zan, H. Kim, S. Li, J. Lee, D. Kang, J. W. Oh, J. Jung, J. K. Shim and C. Park, *Energy Environ. Sci.*, 2024, **17**, 7165–7181.
10 Y. Hu, W. Yang, W. Wei, Z. Sun, B. Wu, K. Li, Y. Li, Q. Zhang, R. Xiao, C. Hou and H. Wang, *Sci. Adv.*, 2024, **10**, eadk4620.
11 C. Guo, H. Tang, P. Wang, Q. Xu, H. Pan, X. Zhao, F. Fan, T. Li and D. Zhao, *Nat. Commun.*, 2024, **15**, 6100.
12 X. Huang, Z. Zheng, H. Wang, W. Xu, M. Wu, M. Wang, C. Chen, L. Wan, R. Du, T. Zhu, Z. Huang, X. Wang, X. Wang, Q. Zhang and X. Jia, *Adv. Funct. Mater.*, 2024, **34**, 2312149.
13 J. Yang, L. Chang, H. Deng and Z. Cao, *ACS Nano*, 2024, **18**, 18980–18991.
14 C. Tang, Y. Yao, M. Li, Y. Wang, Y. Zhang, J. Zhu, L. Wang and L. Li, *Adv. Funct. Mater.*, 2024, 2417207.
15 Z. Liu, Y. Hu, X. Lu, Z. Mo, G. Chen and Z. Liu, *Adv. Energy Mater.*, 2024, **14**, 2402226.
16 H. Jia, X. Jiang, Y. Wang, Y. Lam, S. Shi and G. Liu, *Adv. Energy Mater.*, 2024, **14**, 2304285.
17 Z. Chen, T. Shen, M. Zhang, X. Xiao, H. Wang, Q. Lu, Y. Luo, Z. Jin and C. Li, *Adv. Funct. Mater.*, 2024, **34**, 2314864.
18 D. Lv, S. Zheng, C. Cao, K. Li, L. Ai, X. Li, Z. Yang, Z. Xu and X. Yao, *Energy Environ. Sci.*, 2022, **15**, 2601–2609.
19 X. Zhang, Z. Dai, J. Chen, X. Chen, X. Lin, S. Yang, K. Wu, Q. Fu and H. Deng, *Energy Environ. Sci.*, 2023, **16**, 3600–3611.
20 Y. Huang, H. Cheng, C. Yang, H. Yao, C. Li and L. Qu, *Energy Environ. Sci.*, 2019, **12**, 1848–1856.
21 J. Bai, Y. Huang, H. Wang, T. Guang, Q. Liao, H. Cheng, S. Deng, Q. Li, Z. Shuai and L. Qu, *Adv. Mater.*, 2022, **34**, 2103897.
22 J. Bai, Q. Liao, H. Yao, T. Guang, T. He, H. Cheng and L. Qu, *Energy Environ. Sci.*, 2023, **16**, 3088–3097.
23 Z. Sun, X. Wen, L. Wang, J. Yu and X. Qin, *Energy Environ. Sci.*, 2022, **15**, 4584–4591.
24 Y. Zhang, S. Guo, Z. G. Yu, H. Qu, W. Sun, J. Yang, L. Suresh, X. Zhang, J. J. Koh and S. C. Tan, *Adv. Mater.*, 2022, **34**, 2201228.